Nano-Micro Letters
e-ISSN 2150-5551
CN 31-2103/TB
ARTICLE
https://doi.org/10.1007/s40820-022-00893-7

Cite as
Nano-Micro Lett.
(2022) 14:163

Received: 2 May 2022
Accepted: 7 June 2022

Molybdenum Oxynitride Atomic Nanoclusters Bonded in Nanosheets of N-Doped Carbon Hierarchical Microspheres for Efficient Sodium Storage

Xiaona Pan[1], Baojuan Xi[1] ✉, Huibing Lu[1], Zhengchunyu Zhang[1], Xuguang An[2], Jie Liu[3], Jinkui Feng[4], Shenglin Xiong[1] ✉

HIGHLIGHTS

- $MoO_{2.0}N_{0.5}$ atomic nanoclusters bonded on nanosheets of N/C hierarchical hollow microsphere are synthesized via a facile self- templating strategy.
- Introduction of $MoO_{2.0}N_{0.5}$ atomic nanoclusters benefits the enhancement of electrochemical kinetic.
- Composite of $MoO_{2.0}N_{0.5}$/NC shows excellent electrochemical performance as an anode material for sodium-ion batteries.

ABSTRACT Transition metal nitrides have attracted considerable attention as great potential anode materials due to their excellent metallic conductivity and high theoretical specific capacity. However, their cycling performance is impeded by their instability caused by the reaction mechanism. Herein, we report the engineering and synthesis of a novel hybrid architecture composed of $MoO_{2.0}N_{0.5}$ atomic nanoclusters bonded in nanosheets of N-doped carbon hierarchical hollow microspheres ($MoO_{2.0}N_{0.5}$/NC) as an anode material for sodium-ion batteries. The facile self-templating strategy for the synthesis of $MoO_{2.0}N_{0.5}$/NC involves chemical polymerization and subsequent one-step calcination treatments. The design is beneficial to improve the electrochemical kinetics, buffer the volume variation of electrodes during cycling, and provide more interfacial active

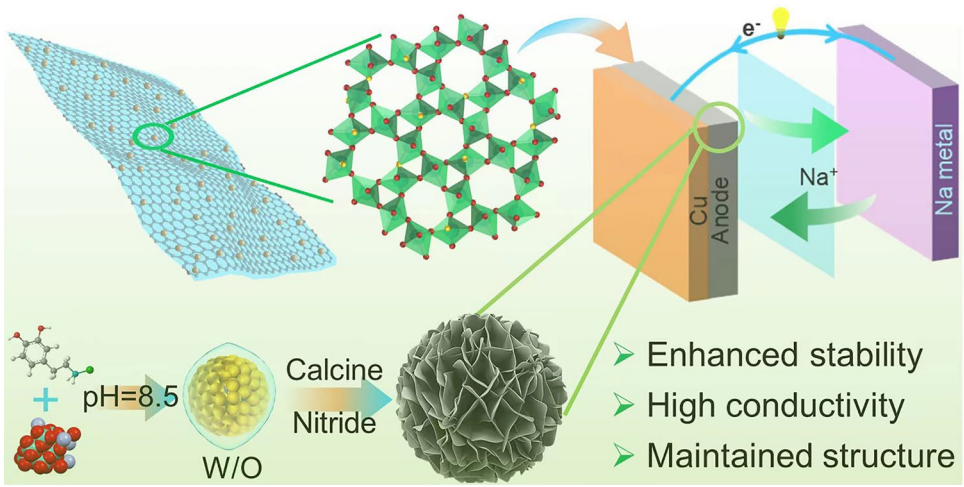

✉ Baojuan Xi, baojuanxi@sdu.edu.cn; Shenglin Xiong, chexsl@sdu.edu.cn
[1] School of Chemistry and Chemical Engineering, State Key Laboratory of Crystal Materials, Shandong University, Jinan 250100, People's Republic of China
[2] School of Mechanical Engineering, Chengdu University, Chengdu 610106, People's Republic of China
[3] The State Key Laboratory of High Performance Ceramics and Superfine Microstructure, Shanghai Institute of Ceramics, Chinese Academy of Sciences, Shanghai 200050, People's Republic of China
[4] School of Materials Science and Engineering, Shandong University, Jinan 250100, People's Republic of China

Published online: 13 August 2022

sites for sodium uptake. Due to these unique structural and compositional merits, these $MoO_{2.0}N_{0.5}$/NC exhibits excellent sodium storage performance in terms of superior rate capability and stable long cycle life. The work shows a feasible and effective way to design novel host candidates and solve the long-term cycling stability issues for sodium-ion batteries.

KEYWORDS Molybdenum oxynitride; Atomic nanocluster; Hollow microspheres; Sodium-ion batteries

1 Introduction

In recent years, sodium-ion batteries (SIBs) have undergone rapid development due to ultra-low-cost and abundant sodium sources, similar physicochemical properties as lithium metal, and low reduction potential, which could provide a competitive alternative to lithium storage systems [1, 2]. The recognition will become increasingly significant because of the diminution of economically attractive lithium sources [3, 4]. Taking inspiration from lithium storage, the scientific community has developed various anode material in past decades [5–8]. Graphite is the most promising anode materials for lithium energy storage [9, 10]. However, Na-ion requires enormous C-atoms to form a stable intercalation compound (e.g., NaC48, NaC64, NaC80) during intercalating into the graphene anode, resulting in an unpractical low reversible capacity [11]. Compared with graphite anodes, metal compounds exhibit intriguing reversible capacity because these compounds could store Na-ion by alloying and conversion reactions [12]. Moreover, these materials would consume fewer electrolytes than the carbon-based anodes due to their high mass density.

Recently, the molybdenum (Mo) compounds have been widely investigated because that among all these metal compounds, Mo-based compounds exhibit favorable crystal structure, considerable capacity low toxicity, and easily fabricated, especially good electrical conductivity [13, 14]. However, bare Mo-based compounds usually deliver inferior rate performance and short lifespan due to their insufficient electrical conductivity and huge volume expansion during the charging/discharging process. To solve these drawbacks, many modified methods have been developed, including constructing pore structures and hollow structures, which can promote the ion diffusion kinetic and suppress the volume expansion [15, 16]. Meanwhile, carbon-modified Mo-compounds could provide fast electron transport pathway, and the heteroatoms doping can increase their intrinsic conductivity and extremely facilitate the kinetics of Mo-based electrodes [17, 18]. Intriguingly, Mo-based nitrides have aroused considerable attention because of their high theoretical specific capacity and excellent electrical conductivity [19, 20]. Till now, however, the most synthesized Mo-based nitrides are in form of thin films, nanoparticles, nanowires, and nanobelts, which are different from metal oxides and metal sulfides with abundant nanostructures morphology. Although these 0- to 2-dimensional (0–2D) types of Mo-based nitrides display enhanced electrochemical properties, these materials still deliver unsatisfactory specific capacity and electrochemical properties owing to their inferior specific surface area and long transport paths of sodium ion during applying as SIBs anode [19, 21]. Consequently, the introduction of three-dimension (3D) porous nanostructure into Mo-based nitrides could be expected to further enhance their electrochemical properties and electrical conductivity.

A crucial strategy to solve inherent issues of SIBs and achieve better performance is to utilize nanostructured anode materials. Compared with traditional nanomaterials, atomic nanoclusters show excellent strongly active, huge surface expose, and low surficial atoms coordinate and have been remarkably used in energy storage and conversion system [22, 23]. To date, however, the nanocluster-based anode materials, which are atom-discernable but not a group of nanoparticle assemblages, have yet to study for the electrode preparation for SIBs. Herein, we designed and synthesized a composite of $MoO_{2.0}N_{0.5}$ atomic nanoclusters and N-doped carbon hierarchical hollow microspheres ($MoO_{2.0}N_{0.5}$/NC), which was featured by atom-defined $MoO_{2.0}N_{0.5}$ atomic nanoclusters anchored on the surface of N-doped carbon nanosheets. As-prepared $MoO_{2.0}N_{0.5}$/NC hollow microspheres as anode displayed some preponderances. First, $MoO_{2.0}N_{0.5}$ atomic nanoclusters played an important role in enhancement of electrochemical kinetic. Second, the constructed N-doped carbon hollow microspheres were exposed to more surface-active sites to mobilize the ions and shorten the Na-ion diffusion distance. Meanwhile, the inherent excellent electrical conductivity and improved rapid electron transfer jointly facilitated the reaction kinetics of desodiation/sodiation. As a result, the $MoO_{2.0}N_{0.5}$/NC composite anode displayed significantly enhanced electrochemical

 https://doi.org/10.1007/s40820-022-00893-7

performance with high capacity, excellent rate performance, long-term cycling stability, and a great opportunity for high-performance SIBs.

2 Experimental

2.1 Sample Preparation

2.1.1 Synthesis of Mo-Polydopamine Hybrid

2 mmol ammonium molybdate tetrahydrate ($(NH_4)_6Mo_7O_{24}{\cdot}4H_2O$, AMT) and 1.6 mmol dopamine hydrochloride (DMH) were dissolved in 80 mL deionized water and stirred. After 30 min continues stirring, 150 mL ethanol was added into the mixture, and the pH was held constantly at 8.5 ± 0.1 by ammonium hydroxide to turn the base solution frequently and stirred for 2 h. The dark red precipitation was collected by centrifugation, washed with ethanol for three times, and finally filtrated and dried in a vacuum oven at 60 °C for 24 h.

2.1.2 Fabrication of $MoO_{2.5}$ /NC Microsphere

Mo-polydopamine hybrid was placed in a tube furnace with an Al_2O_3-boat. The tube furnace was heated at 600 °C for 3 h with a heating rate of 5 °C min^{-1} in Ar flow, and then naturally cooled down to 20 °C.

2.1.3 Fabrication of $MoO_{2.0}N_{0.5}$/NC Microsphere

The obtained $MoO_{2.5}$/NC and C_3N_4 were mixed into ethanol with a weight ratio of 1/5, and grinded with a glass rod. Then, the mixture was dried at 60 °C for 6 h. The dried mixture was placed in a tube furnace and heated at 600 °C for 3 h in Ar atmosphere with a heating rate of 5 °C min^{-1}.

2.2 Materials Characterization

The morphologies and structures of the prepared materials were performed on a Gemini 300 field emission scanning electron microscope (SEM) with an accelerated voltage of 5 kV and a field emission transmission electron microscope (TEM, JEOL JEM-ARM 200F, FEI TalosF200x) operated at 200 kV with a field-emission scanning electron microscope (EDS, super-X EDS) at 5 kV. The crystalline structures of the products were conducted by X-ray diffraction (XRD) with a wavelength of 1.5418 Å. The nitrogen adsorption-desorption isotherm was carried out to obtain the texture properties of the products at 77 K on a Micromeritics analyzer (ASAP-2000 HD 88). Thermogravimetric analysis (TGA) was applied to test the carbon content of the products by heating specimen from room temperature to 650 °C with a rate of 10 °C min^{-1} under the air flow on a TA instrument (Mettler Toledo TGA/SDTA851). Raman spectra of the products were performed on a confocal laser micro-Raman spectrometer (JY LABRAM-HR) with a wavelength of 514.5 nm. FT-IR spectra were measured on a Fourier transform infrared spectrometer (FT-IR, Bruker, Tensor II) in a wavenumber range of 400–4000 cm^{-1}. The composition of the products was detected on an X-ray photoelectron spectroscopy (XPS, Thermo ESCALAB 250Xi). The C 1 *s* peak at 284.8 eV is the reference.

2.3 Cell Performance Testing

The $MoO_{2.5}$/NC and $MoO_{2.0}N_{0.5}$/NC electrodes were prepared by mixing a slurry of $MoO_{2.5}$/NC (or $MoO_{2.0}N_{0.5}$/NC), carboxy methyl cellulose (CMC), and carbon black with a mass ratio of 8/1/1 in the N-methyl-2-pyrrolidone (NMP) solvent. The slurry was cast onto a Cu foil (purity: 99.95%, Alfa Aesar, China) with a thickness of 15 μm. Then, the anode electrodes were transferred into a vacuum oven to dry at 80 °C for overnight. The anode electrodes were punched into 12-mm-diameter round disk and transferred into an Ar-filled glovebox ($O_2 < 0.1$ ppm, $H_2O < 0.1$ ppm). The mass loading of active materials of $MoO_{2.5}$/NC (or $MoO_{2.0}N_{0.5}$/NC) was around 1.5 g cm^{-2}. The coin cells were assembled in a glovebox with Ar-filled, where sodium foil was counter and reference electrode, glass fiber was separator, and 1 M $NaClO_4$/5 vol% fluoroethylene carbonate (FEC)/ethylene carbonate (EC) -diethylene carbonate (DEC) (v/v = 1/1) as electrolytes. The sodium-ion batteries were galvanostatic charged/discharged on a Land-CT2001A in the range of 0.1–3 V (*vs.* Na^+/Na) with a various current density of 0.1–20 A g^{-1}. All coin cells were activated for three cycles at 0.1 A g^{-1} before high current density. Potentiostat electrochemical impedance spectroscopy (EIS) was used to investigate the resistance of coin cells with a frequency range between 0.01 Hz and 100 kHz and an AC amplitude of

5 mV. The EIS was performed on the sodium-ion batteries before and after various cycles with a current density of 1 A g^{-1}. Cyclic voltammetry (CV) was measured on a CHI760E electrochemical workstation in a voltage range of 0.1–3 V (*vs*. Na^+/Na).

3 Results and Discussion

3.1 Physical Characterization

The composite of $MoO_{2.0}N_{0.5}$/NC hollow microsphere is synthesized by a simple polymerization at room temperature combined with calcination, wherein $MoO_{2.0}N_{0.5}$ atomic nanoclusters are uniformly distributed on the nanosheets of the N-doped carbon hierarchical hollow microsphere. The schematic diagram of the fabrication process is illustrated in Fig. 1a. As shown in Fig. 1a, we mix ammonium molybdate and dopamine hydrochloride in an aqueous solution with a molar ratio of 8:1, which shows a clarified solution with orange–red color. The dopamine HCl is chelated with molybdate-ion. Mo-dopamine chelate has very low solubility in ethanol. Thus, with the addition of ethanol, H_2O/ethanol interface is gradually formed, where the hydrophobic groups of Mo-dopamine chelate toward ethanol and the hydrophilic groups orient inward water, and the solution turns to orange–yellow suspension. With ammonia added into the solution to adjust the pH, the self-polymerization of the dopamine is initiated along the water/ethanol interface.

Mo-polydopamine hybrid (precursor) is synthesized by mixing AMT and DMH. Polydopamine as a carbon source is prepared under alkaline conditions via adding ammonium hydroxide. The molecular of dopamine hydrochloride has plenty of amino and catechol groups, which can form chelate components with transition metal ions and metal oxyanions by the polymerized reaction [24]. FT-IR spectra of DMH and precursor are shown in Fig. 1b (full spectra in Fig. S1). It is observed that DMH has an absorption band at 1342 and 1320 cm^{-1}, which can be attributed to the CH_2 and C-O–H bending vibration, while the absorption band at 1189 and 1174 cm^{-1}, which can be assigned to the C-O and C–C stretching vibration, separately [25]. For the Mo-polydopamine hybrid, there are plenty of catechol and amino groups that can chelate transition-metal ion and metal-containing oxyanion by self-polymerization can be observed in FT-IR spectra. Moreover, the new absorption bands at 1538 and 1433 cm^{-1} emerge, which indicates that an indole structure is formed [25, 26]. To obtain $MoO_{2.0}N_{0.5}$/NC, Mo-polydopamine hybrid is calcined at elevated temperature on a tube furnace under an Ar flow. For comparison, $MoO_{2.5}$/NC was also synthesized in the same condition without addition of C_3N_4. The synthesis detail is explained in the experimental section.

The crystallinity of prepared $MoO_{2.5}$/NC and $MoO_{2.0}N_{0.5}$/NC is demonstrated by the XRD. As shown in Fig. 1c, both $MoO_{2.5}$/NC and $MoO_{2.0}N_{0.5}$/NC display a broaden peak at 25.3°, which is attributed to carbon. It can be observed in Fig. 1c that $MoO_{2.5}$/NC is a crystalline material and there is amount of carbon content resulting in a series of weak crystalline peaks. While mixed $MoO_{2.5}$/NC with C_3N_4 to introduce N atoms into $MoO_{2.5}$/NC, the crystal phase of product $MoO_{2.0}N_{0.5}$/NC is changed to an amorphous material [27]. Figure 1d represents the Raman spectra of $MoO_{2.5}$/NC and $MoO_{2.0}N_{0.5}$/NC to analyze the defects and graphitization. There are two strong peaks at ~ 1356 and ~ 1584 cm^{-1}, corresponding to D-bond and G-bond of carbon. Generally, the degree of defects of carbon materials is verified by the intensity ratio of I_D/I_G [28, 29]. Here, a higher value of I_D/I_G of $MoO_{2.0}N_{0.5}$/NC represents that the structure has more active defect sites for intercalation/extraction of Na^+ caused by the introduction of $MoO_{2.0}N_{0.5}$ atomic nanoclusters and heteroatoms [30].

TGA is carried out to determine the $MoO_{2.5}$ and $MoO_{2.5}N_{0.5}$ content in the composite (Fig. 1e). The weight loss before 350 °C can be attributed to oxidation of $MoO_{2.5}$ and $MoO_{2.0}N_{0.5}$ to MoO_3 and NO_2. The carbon content of $MoO_{2.5}$/NC and $MoO_{2.0}N_{0.5}$/NC in the composites is obtained as 53.3% and 62.9%, respectively (the calculation details are shown in Fig. S2). The overall amount of C, N, O, and Mo of $MoO_{2.5}$/NC and $MoO_{2.0}N_{0.5}$/NC is listed in Table S1, which is obtained from the CHN elemental analysis and inductively coupled plasma mass spectrometer (ICP-MS) measurement. The overall amount of C in the $MoO_{2.5}$/NC and $MoO_{2.0}N_{0.5}$/NC is estimated to be 50.7% and 54.4%. More importantly, the amount of N element of $MoO_{2.0}N_{0.5}$/NC is 2.36%, while that of $MoO_{2.5}$/NC is only 0.33%, which is illustrated that N is successfully doped into $MoO_{2.5}$/NC.

To verify the porous structural characterization of $MoO_{2.5}$/NC and $MoO_{2.0}N_{0.5}$/NC, the nitrogen adsorption/desorption measurement is performed and the results are shown in Fig. S3. The N_2-sorption isotherms of $MoO_{2.5}$/NC and $MoO_{2.0}N_{0.5}$/NC are typical type III isotherm. The

 https://doi.org/10.1007/s40820-022-00893-7

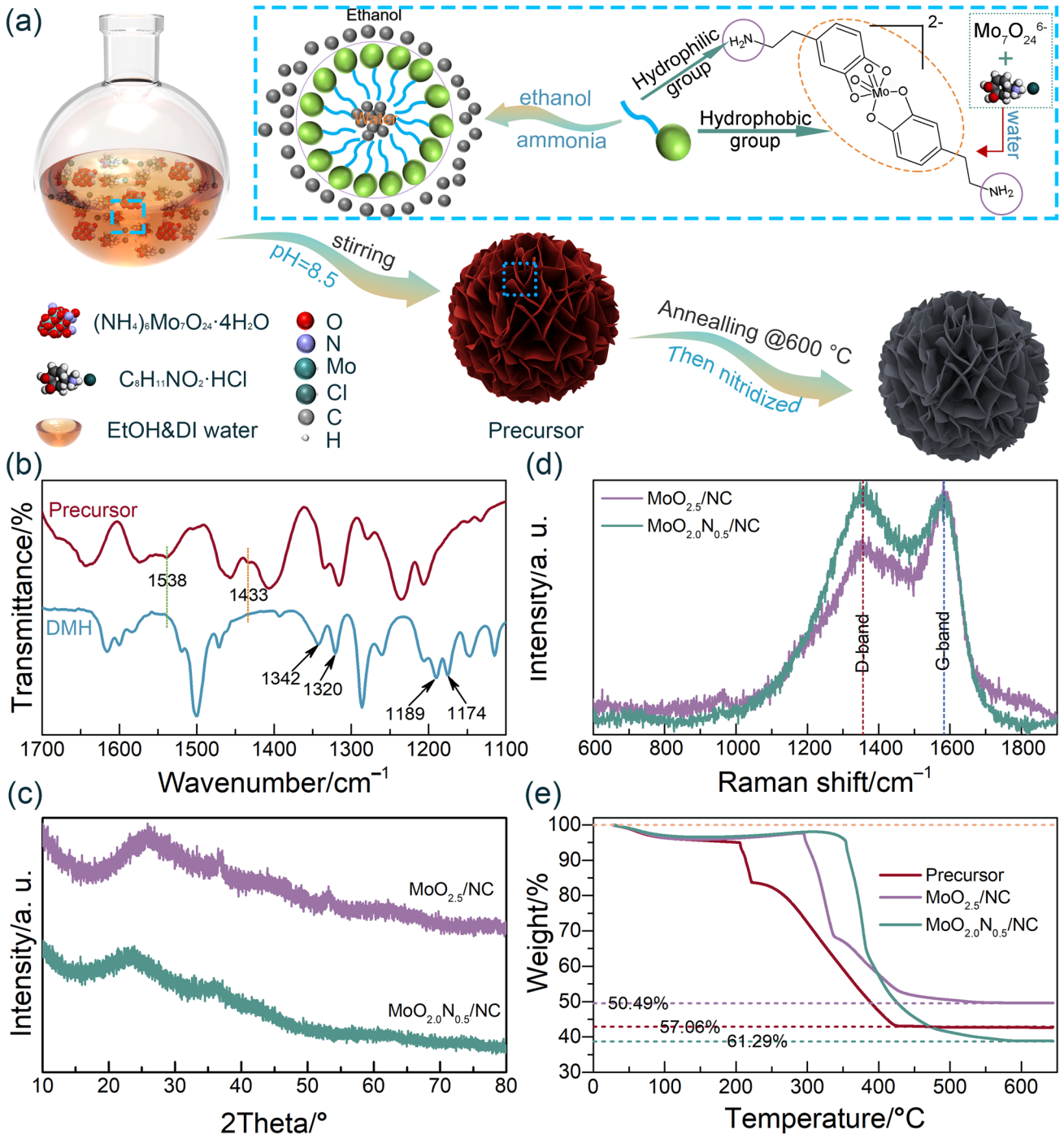

Fig. 1 **a** Scheme of synthesis of $MoO_{2.0}N_{0.5}$/NC hollow microspheres. **b** FT-IR spectra for $MoO_{2.5}$/NC and $MoO_{2.0}N_{0.5}$/NC. **c** XRD patterns and **d** Raman spectra for $MoO_{2.5}$/NC and $MoO_{2.0}N_{0.5}$/NC. **e** TGA curves for precursor (Mo-polydopamine hybrid), $MoO_{2.5}$/NC, and $MoO_{2.0}N_{0.5}$/NC

type-H_3 hysteresis loop appears at a relative pressure P/P_0 over 4.5, indicating that slit-like pores are constructed by flake particles stack. By Brunauer–Emmett–Teller model, the specific surface area of $MoO_{2.0}N_{0.5}$/NC is calculated with a value of 63.4 $m^2\ g^{-1}$, which is higher than that of $MoO_{2.5}$/NC of 42.9 $m^2\ g^{-1}$. It can be explained that the introduction of $MoO_{2.0}N_{0.5}$ atomic nanoclusters effectively facilities the stacking and agglomeration and results in the

formation of porous microspheres. Additionally, Fig. S3d shows the pore size distribution curves according to the Barrett–Joyner–Halenda model. The pore size of both $MoO_{2.5}$/NC and $MoO_{2.0}N_{0.5}$/NC mainly distributes in a range of 3–15 nm and an obvious increase of specific pore volume with N-doping (Fig. S3d). It reveals that $MoO_{2.0}N_{0.5}$/NC has more abundant mesopores than $MoO_{2.5}$/NC. The total pore volume of $MoO_{2.0}N_{0.5}$/NC is 0.36 cm^3 g^{-1}, which is larger than that of $MoO_{2.5}$/NC of 0.26 cm^3 g^{-1}. This can be explained that carbon layers of $MoO_{2.0}N_{0.5}$/NC provide more mesopores and active defect site, which agrees with results of Raman spectra. The $MoO_{2.0}N_{0.5}$/NC micro- and nanostructure has a large specific area and rich mesopores, which is beneficial to increase the contact area between the electrode and electrolytes and improve the penetration of electrolytes [31]. The morphology and detailed microstructure of the as-synthesized $MoO_{2.0}N_{0.5}$/NC are examined by field emission scanning electron microscope (FESEM) and TEM as shown in Fig. 2, while that of precursor and $MoO_{2.5}$/NC is exhibited in Figs. S4 and S5. It is noticed that hierarchical hollow microspheres are synthesized with a size of ~ 1 μm (Fig. S4). Furthermore, the morphologies of the hollow microsphere are perfectly maintained after calcinating at elevated temperatures (Figs. 2a–b and S5). Figures S5 and 2a–b present the morphologies of $MoO_{2.5}$/NC and $MoO_{2.0}N_{0.5}$/NC, indicating high yield hollow microsphere and the unchanged size. FESEM images of precursor and $MoO_{2.5}$/NC and their corresponding energy-dispersive X-ray spectroscopy (EDX) spectrum elemental mapping exhibit that Mo, C, N, and O elements are a uniform spatial distribution throughout the entire hollow microsphere (Figs. S4–S5). As shown in Fig. 2a–c, it is obvious to observe that the $MoO_{2.0}N_{0.5}$/NC is a hollow microsphere and the 3D network of $MoO_{2.0}N_{0.5}$/NC has abundant voids between the nanosheets, which can enhance the contact between the active materials and electrolytes and alleviate the volume expansion. Importantly, the well-defined and ultrafine $MoO_{2.0}N_{0.5}$ nanoparticles are uniformly distributed on the N-doped carbon nanosheets (Fig. 2d). Figure 2e displays the high-resolution TEM image of $MoO_{2.0}N_{0.5}$/NC and reveals that $MoO_{2.0}N_{0.5}$ atom-discernable clusters with evenly uniform sizes without continuous crystal lattice stripes are homogeneously distributed on the N-doped carbon nanosheets, which reveals the lack of long-range atomic structure, *i.e.,* amorphous structure and is consistent with the results of XRD [32]. Furthermore, insert patterns in Fig. 2d of the selected area electron diffraction (SAED) show the weak ring, further indicating that these materials have an amorphous structure. The size of distributed $MoO_{2.0}N_{0.5}$ atomic nanoclusters is further estimated by the atomic-resolution high-angle annular dark-field scanning TEM (HAADF-STEM) images, *i.e.,* ~ 1 nm (Fig. 2f–g). Moreover, some discrete bright dots can be observed in Fig. 2h, indicating that trace single-atom $MoO_{2.0}N_{0.5}$ existed during the calcining process. The STEM image of $MoO_{2.0}N_{0.5}$/NC and corresponding EDX spectrum elemental mapping exhibit that Mo, C, N, and O elements are a homogenous distribution throughout the entire hollow microsphere (Fig. 2i–m). The EDX spectra obtained for an undoped and a N-doped single hollow microsphere show the stoichiometry of Mo/O of 1/2.5 and Mo/O/N of 1/2.0/0.5 (Fig. S6), respectively. Combined with the CHN tests and ICP-MS measurements, the composition is confirmed as $MoO_{2.5}$/NC and $MoO_{2.0}N_{0.5}$/NC. The EDX spectrum from a single N-doped hollow microsphere exhibits a N-atomic percentage of 2.76% (Fig. S6b), which is increased compared to an undoped one.

XPS is carried out to analyze the $MoO_{2.5}$/NC and $MoO_{2.0}N_{0.5}$/NC compositions of elements and their chemical state. As shown in Fig. 3, the elements of C, O, N, and Mo are detected. The XPS survey spectra and high-resolution spectra of common metal in carbon indicate that $MoO_{2.5}$/NC and $MoO_{2.0}N_{0.5}$/NC contain only C, O, N, and Mo without detectable impurity on the surface of the compositions (Fig. 3a). The standard peak of C 1 *s* is at 284.8 eV as the reference. For C 1 *s* and O 1 *s* spectra, the peaks at 286.1 and ~ 532.5 eV are attributed to C-O bond. The new peaks at 288 and 399.8 eV of $Mo_{2.0}N_{0.5}$/NC hollow microsphere are assigned to the sp^2-bond N in triazine rings (C-N = C) [33]. The fitting peak of O 1 *s* binding energy is concerned at 530.5 eV, which is typical for Mo–O coordination, indicating the MoO_x (x = 2 ~ 3) components form on the surface [34]. For high-resolution XPS spectra of N 1 *s* and Mo 3*p* (Fig. 3d), the distinct N and Mo could be deconvoluted into three peaks for $MoO_{2.5}$/NC and $MoO_{2.0}N_{0.5}$/NC, illustrating the presence of diverse chemical states of N and Mo. The peak at binding energy of 400.4, 399.8, 398.4, 396.4, and 395.8 eV can be assigned to the N 1 *s* satellite, C–C = N, Mo–O, Mo–O, and Mo–N bonds [35]. As shown in Fig. 3e, high-resolution XPS spectra of Mo 3d exhibits two characteristic peaks of Mo^{6+} $3d_{3/2}$ and Mo^{6+} $3d_{5/2}$ centered at 232.9 and 236.0 eV, respectively. The results correspond to the standard XPS spectrum for MoO_x (x = 2 ~ 3) (Mo^{4+} $3d_{5/2}$ at

 https://doi.org/10.1007/s40820-022-00893-7

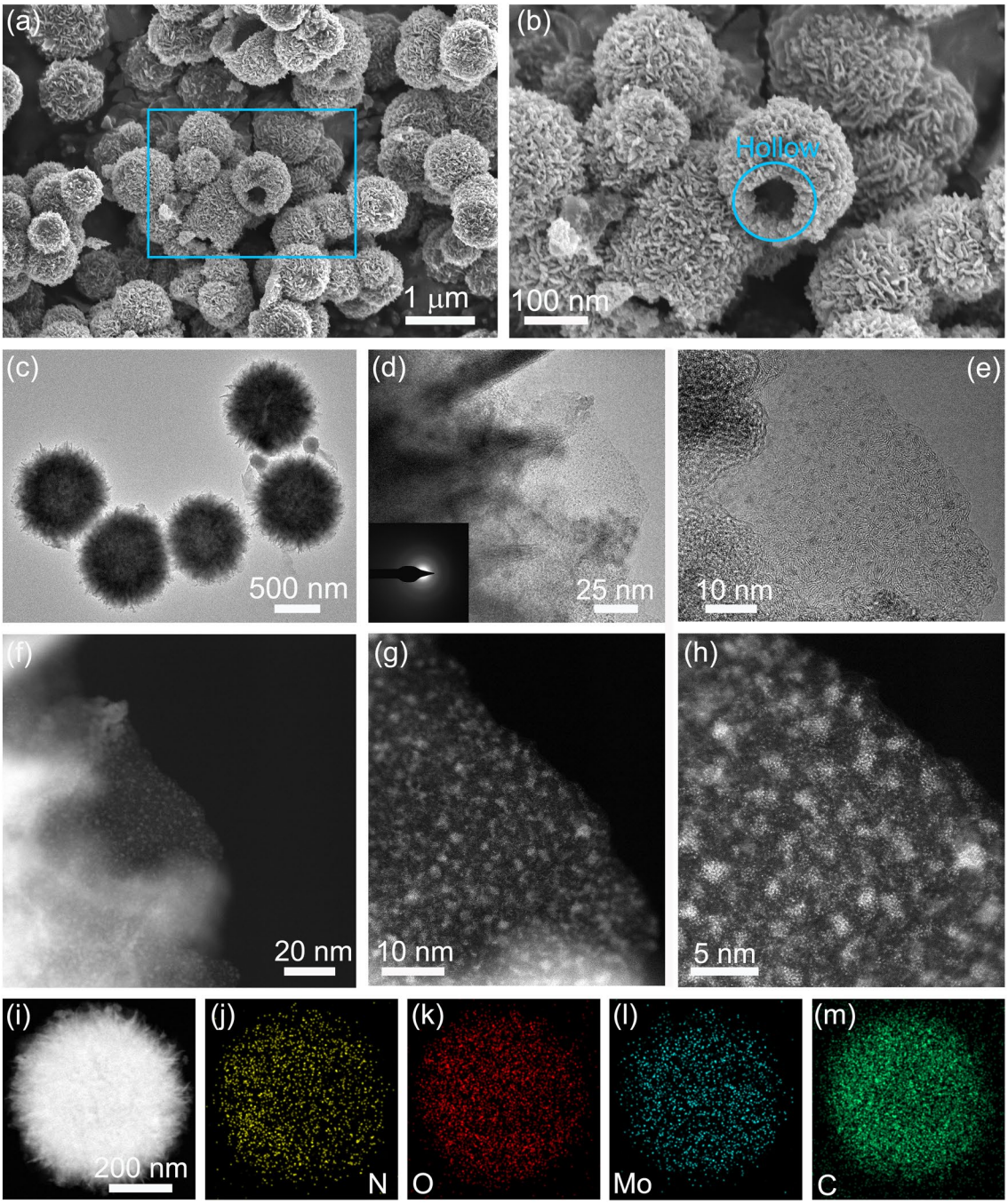

Fig. 2 Morphological and structural characterization of $MoO_{2.0}N_{0.5}$/NC. **a, b** FESEM images. **c** TEM images. **d, e** HRTEM images. **f–h** HAADF-STEM images. **i** STEM image, and the corresponding EDX mappings of **j** N, **k** O, **l** Mo, and **m** C. The insert in **d** is the SAED pattern of $MoO_{2.0}N_{0.5}$/NC

232.4 eV, Mo^{6+} $3d_{5/2}$ at 236.0 eV) [36]. For $MoO_{2.0}N_{0.5}$/NC materials, the new peaks at 230.2 and 233.5 eV can also be observed, which are attributed to Mo^{5+} $3d_{3/2}$ and Mo^{5+} $3d_{5/2}$, separately [37]. On the surface of the hollow microsphere $MoO_{2.0}N_{0.5}$/NC, there is amount of Mo^{5+} appears after N-doped, indicating that the $MoO_{2.0}N_{0.5}$ atomic nanoclusters have been successfully introduced into nanosheets of NC hollow microspheres.

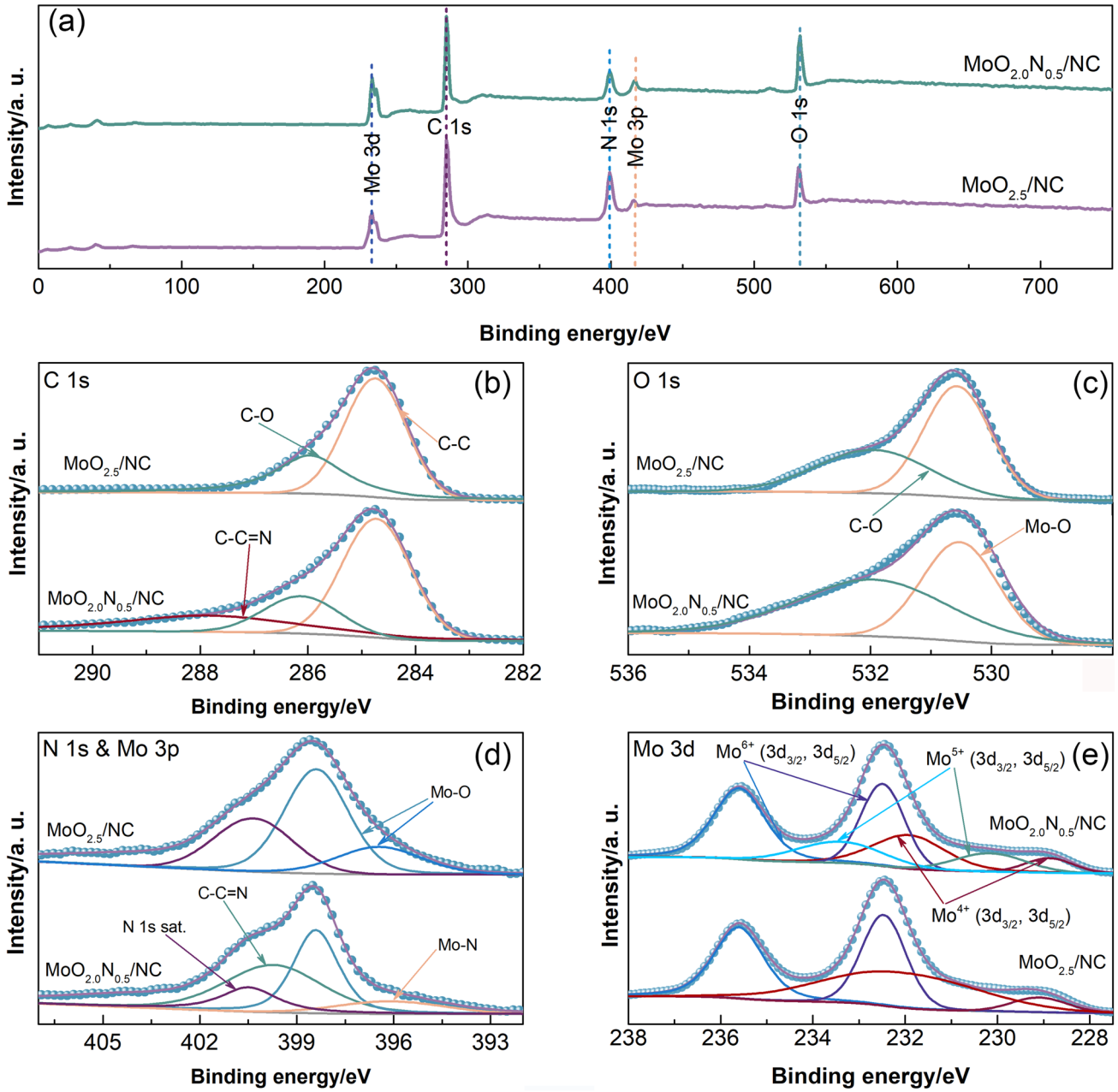

Fig. 3 **a** XPS spectra of $MoO_{2.5}$/NC and $MoO_{2.0}N_{0.5}$/NC; high-resolution XPS spectra of C **b** 1 *s*, **c** O 1 *s*, **d** N 1 *s* & Mo 3*p*, and **e** Mo 3*d*

3.2 Electrochemical Results

To demonstrate the effect of $MoO_{2.0}N_{0.5}$ atomic nanoclusters and heteroatoms in the anode materials for mobilizing ions, the kinetics behaviors of $MoO_{2.5}$/NC and $MoO_{2.0}N_{0.5}$/NC are systematically explored for SIBs. Figure 4a-b displays the initial CV curves of the $MoO_{2.5}$/NC and $MoO_{2.0}N_{0.5}$/NC as electrodes with various scan rates of 0.01–1 mV s^{-1} in a voltage range between 0.1 and 3.0 V (*vs.* Na^+/Na). The reaction kinetics of $MoO_{2.0}N_{0.5}$/NC in SIBs are investigated by CV tests with various scan rates (υ). The power-law formula has been used to qualitatively analyze the capacitance effect. The peak current density (*i*) has a relationship with the scan rate *υ* as an equation of $i = a\upsilon^b$ [37, 38]. The value of *b* can be calculated by the function of log(*i*) and log(*υ*). The curves of log(*i*)–log(*υ*)

https://doi.org/10.1007/s40820-022-00893-7

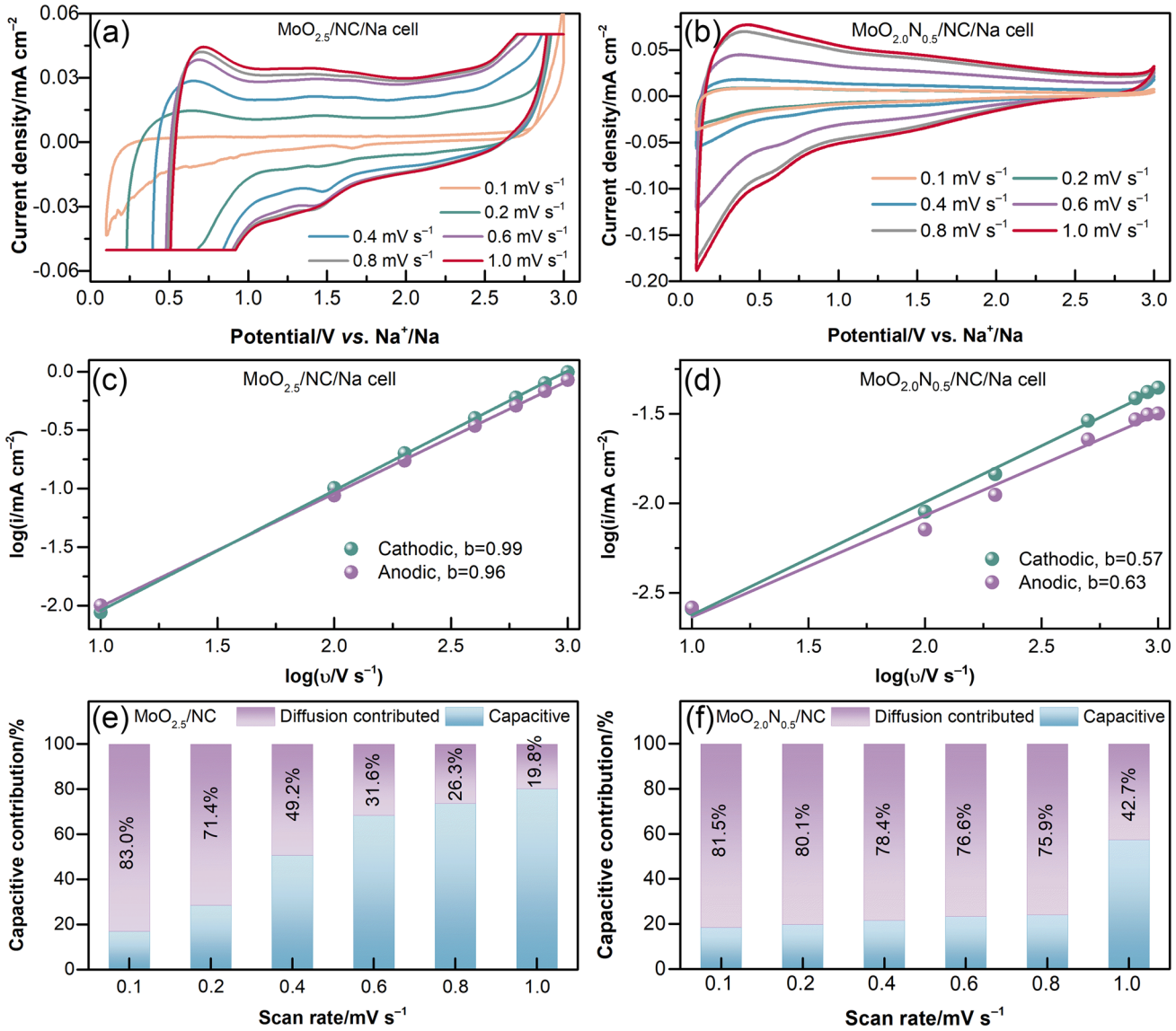

Fig. 4 Kinetics analysis of the $MoO_{2.5}$/NC and $MoO_{2.0}N_{0.5}$/NC electrode. CV curves for **a** $MoO_{2.5}$/NC/Na cells and **b** $MoO_{2.0}N_{0.5}$/NC/Na cells with a various scan rate. *b*-value analysis using the relationship between the anodic and cathodic peak currents and scan rates: **c** $MoO_{2.5}$/NC and **d** $MoO_{2.0}N_{0.5}$/NC. Contribution ratio of the capacitive and diffusion-controlled at various scan rate for **e** $MoO_{2.5}$/NC and **f** $MoO_{2.0}N_{0.5}$/NC anodes

of $MoO_{2.5}$/NC and $MoO_{2.0}N_{0.5}$/NC electrodes are shown in Fig. 4c-d, respectively. The *b* values of the cathodic and anodic peaks are obtained and the values are between 0.5 and 1, illustrating a mixed mechanism [39]. Particularly, the cathodic and anodic *b* values of $MoO_{2.0}N_{0.5}$/NC are around 0.6, indicating the increase of the diffusion-controlled contribution with the introduction of heteroatoms, which probably results in enhanced ion diffusion. Moreover, the diffusion-controlled contribution ($k_1\upsilon$) and capacitive contribution ($k_2\upsilon^{1/2}$) are the current response i_r at a fixed voltage V and estimated by the following equation: $i_r(V) = k_1\upsilon + k_2\upsilon^{1/2}$ [40]. By obtaining the value of k_1 and k_2, the $i_r(V)$ can be calculated and divided into two parts, *i.e.,* diffusion-controlled k_1 and capacitor-controlled k_2. The capacitive contribution ratio at various scan rates is summarized in Figs. 4e–f and S7 provides the capacitive contribution ratio at 0.1 mV s^{-1}. It is observed that the distributive capacitance of $MoO_{2.0}N_{0.5}$/NC is lower than that

of $MoO_{2.5}$/NC, which is further revealed that $MoO_{2.0}N_{0.5}$/NC electrodes have improved Na-ion diffusion.

The electrochemical characterization of $MoO_{2.0}N_{0.5}$/NC electrode is investigated by CV with a scan rate of 0.1 mV s^{-1} in a voltage range of 0.1–3 V (*vs.* Na^+/Na) for the initial three cycles in Fig. S8. The CV curves show the initial prominent peaks centered at ~ 0.7 and 0.4 V, which is related to sodium-ion intercalation into $MoO_{2.0}N_{0.5}$ to form $Na_xMoO_{2.0}N_{0.5}$ phase and the formation of solid electrolytes interphase (SEI) layers when $MoO_{2.0}N_{0.5}$/NC is employed as an anode for SIBs (shown in Fig. S8) [41–45]. The initial irreversible capacity of $MoO_{2.0}N_{0.5}$/NC electrode results from the formation of SEI layer, the decomposition of the electrolytes, and the irreversible sodium-ion insertion. As shown in Fig. S8, a cathodic peak at ~ 0.1 V and an anodic peak at 0.2 V can be ascribed to the sodium-ion intercalation and de-intercalation, respectively [46–48]. Furthermore, the initial anodic scan shows a several peaks between 1.2 ~ 1.8 V, which is caused by the multistep de-intercalation of $Na_xMoO_{2.0}N_{0.5}$ to $MoO_{2.0}N_{0.5}$. After the initial cycle, the nearly overlapped CV curves of $MoO_{2.0}N_{0.5}$/NC electrode in SIBs demonstrate the high cycling reversibility, which can be attributed to N-doped.

Furthermore, Fig. S9 shows d*q*/d*V* curves of the $MoO_{2.5}$/NC and $MoO_{2.0}N_{0.5}$/NC as electrodes in a voltage range of 0.1–3 V. During the initial cycle of $MoO_{2.0}N_{0.5}$/NC cells, we found three stages of sodiation at ~ 0.7, 1.1 V; while there are four stages of sodiation at ~ 0.6, 0.9, 1.1, 2.5 V for $MoO_{2.5}$/NC cells (observed on Fig. S9a–b). Interestingly, after the initial cycle, the sodiation stage changes to ~ 0.7 V, suggesting that the electrodes undergo irreversible reactions during the initial discharge; however, the reaction observed in further cycles is highly reversible. Importantly, the initial d*q*/d*V* curve of $MoO_{2.0}N_{0.5}$/NC exhibits less irreversible reactions, indicating that it is a more stable anode material for sodium storage.

The successful synthesis of the $MoO_{2.0}N_{0.5}$/NC for a superior SIB anode material is evident from the excellent electrochemical behavior (Fig. 5). Figure 5a–b displays the galvanostatic voltage profiles of $MoO_{2.5}$/NC and $MoO_{2.0}N_{0.5}$/NC at initial cycles with a current density of 0.1 A g^{-1}, thereby suggesting $MoO_{2.0}N_{0.5}$/NC has high reversibility. Furthermore, the results demonstrate that the sloping electrochemical curves of $MoO_{2.0}N_{0.5}$/NC are analogous to those materials, which exhibit a solid-solution behavior, *i.e.,* single-phase reaction [49]. The initial charge capacity of $MoO_{2.0}N_{0.5}$/NC is 321.0 mAh g^{-1}, which is higher than that of $MoO_{2.5}$/NC of 134.6 mAh g^{-1}. In the initial cycles, the side reaction is dominantly attributed to the decomposition of the electrolyte forming the SEI layer on the electrode surface. Specifically, the activation process can present low initial Coulombic efficiency (CE). Figure 5c exhibits the cycling performance of the $MoO_{2.0}N_{0.5}$/NC electrode in the voltage range of 0.1–3 V (*vs.* Na^+/Na) with a current density of 0.1 A g^{-1}. The results indicate highly reversible capacity and distinct characteristics. The cycling performance reveals an ultra-stable cyclability over 500 cycles at 0.1 A g^{-1} and a CE approach 100% except for initial cycles. The cyclability of $MoO_{2.0}N_{0.5}$/NC significantly exceeded that of $MoO_{2.5}$/NC anode at 0.1 A g^{-1} due to the introduction of $MoO_{2.0}N_{0.5}$ atomic nanoclusters.

To further evaluate the electrochemical properties of the $MoO_{2.0}N_{0.5}$/NC electrode, the C-rate performance and long-term cycling performance are conducted by galvanostatic charge/discharge with various currents (shown in Figs. 5d–e and S10). In the last 5 cycles of each current, reversible charge specific capacity of 360.4, 317.6, 270.8, 224.3, 189.0, 101.1, 76.8, 76.8, and 68.5 mAh g^{-1} is observed at 0.1, 0.2, 0.5, 1, 2, 5, 10, 15, and 20 A g^{-1}, respectively. It is notable that when the current is reverted to 0.1 A g^{-1} after 45 cycles, the capacity is restored to the early stage. The excellent rate capability characterizations are ascribed to the metallic electron-conductivity of transition metal nitride, the unique ordered mesoporous structure, and the introduction of $MoO_{2.0}N_{0.5}$ atomic nanoclusters [50]. More importantly, the $MoO_{2.0}N_{0.5}$/NC electrode also indicates exceptional cycling stability even at higher current densities. The rate cyclability of $MoO_{2.0}N_{0.5}$/NC significantly exceeded that of $MoO_{2.5}$/NC (Fig. 5d) and carbonaceous [49] anode materials. As shown in Fig. 5e, the as-fabricated electrode exhibits a high capacity of 83.3 mAh g^{-1} and 79.2 mAh g^{-1} after 10,000 cycles at 10 and 15 A g^{-1}, respectively, without noticeable capacity fading. After long-term cycles, the sodium-ion cells are disassembled in an Ar-filled glovebox. The coin cell case, sodium metal electrode, and separators of $MoO_{2.5}$/NC cells display a dark-black color due to amounts of side-reactions, which is the main reason that the cells cannot deliver the expected capacity, while these of $MoO_{2.0}N_{0.5}$/NC cells have neglected changes, *i.e.,* less side-reaction, leading to significantly battery performance (Fig. S11 and insert of Fig. 5e). The hollow microsphere structure of $MoO_{2.0}N_{0.5}$/NC is well maintained after long-term cycling, indicating

 https://doi.org/10.1007/s40820-022-00893-7

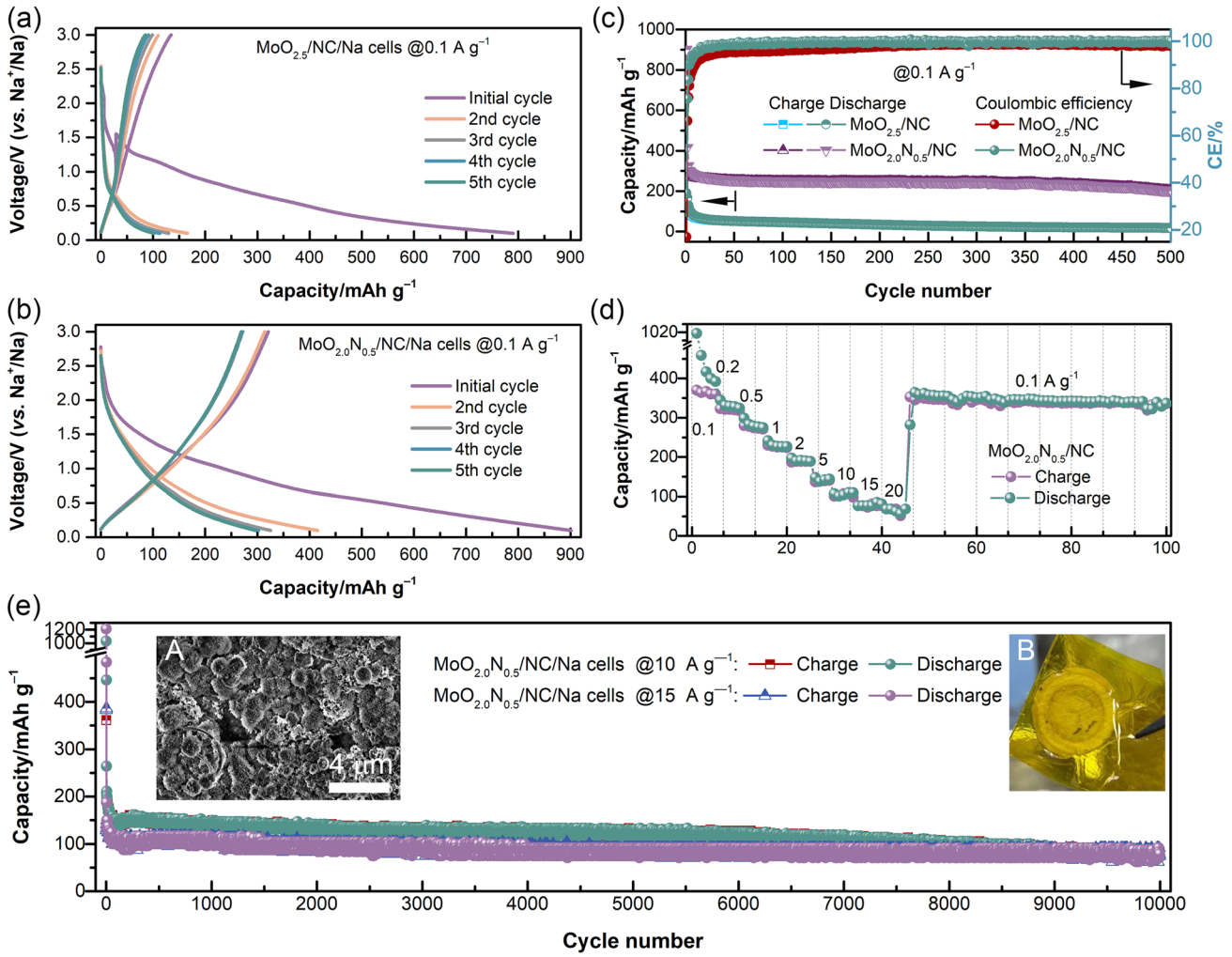

Fig. 5 Electrochemical performance of $MoO_{2.0}N_{0.5}$/NC electrode. Initial charge and discharge cycles of **a** $MoO_{2.5}$/NC and **b** $MoO_{2.0}N_{0.5}$/NC. **c** Cycling performance of $MoO_{2.5}$/NC and $MoO_{2.0}N_{0.5}$/NC. **d** Rate cycling performance of $MoO_{2.0}N_{0.5}$/NC. **e** Long-term cycling performance at current densities of 10 and 15 A g^{-1}. The insert figures of **e** shown **A** the SEM image of $MoO_{2.0}N_{0.5}$/NC electrode after 10,000 cycles at 10 A g^{-1} and **B** the digital picture of separator faced $MoO_{2.0}N_{0.5}$/NC electrode side. The $MoO_{2.0}N_{0.5}$/NC cell was disassembled after 10,000 cycles at 10 A $g.^{-1}$

that the $MoO_{2.0}N_{0.5}$/NC as an anode shows superior stability during sodium-ion intercalation/de-intercalation (insert A of Fig. 5e). The results reveal that $MoO_{2.0}N_{0.5}$/NC anode shows excellent stability against the electrolytes and results in superior rate capability and long lifespan, which could be a feasible candidate for energy storage fields since it is economically competitive (Table S2). Table S2 lists a comparison of rate capacity of carbonaceous materials for SIBs, which indicates that battery performance of $MoO_{2.0}N_{0.5}$/NC is superior to the most Mo-based anode materials.

To analyze the electrochemical kinetics of the $MoO_{2.5}$/NC and $MoO_{2.0}N_{0.5}$/NC materials, galvanostatic intermittent titration technique (GITT) and EIS are conducted, and the results display in Fig. 6. The results of GITT test provide that the diffusion coefficient of Na^+ of $MoO_{2.5}$/NC and $MoO_{2.0}N_{0.5}$/NC electrode during charging/discharging is 10^{-10}–10^{-8} cm^2 s^{-1}. It can be observed that the diffusion coefficient of sodium ion of $MoO_{2.0}N_{0.5}$/NC electrode is considerably much higher than that of $MoO_{2.5}$/NC electrode. The strong dynamic features of $MoO_{2.0}N_{0.5}$/NC materials are probably due to the unique structure with $MoO_{2.0}N_{0.5}$ atomic nanocluster introducing and N-doping that can promote the Na^+ migration.

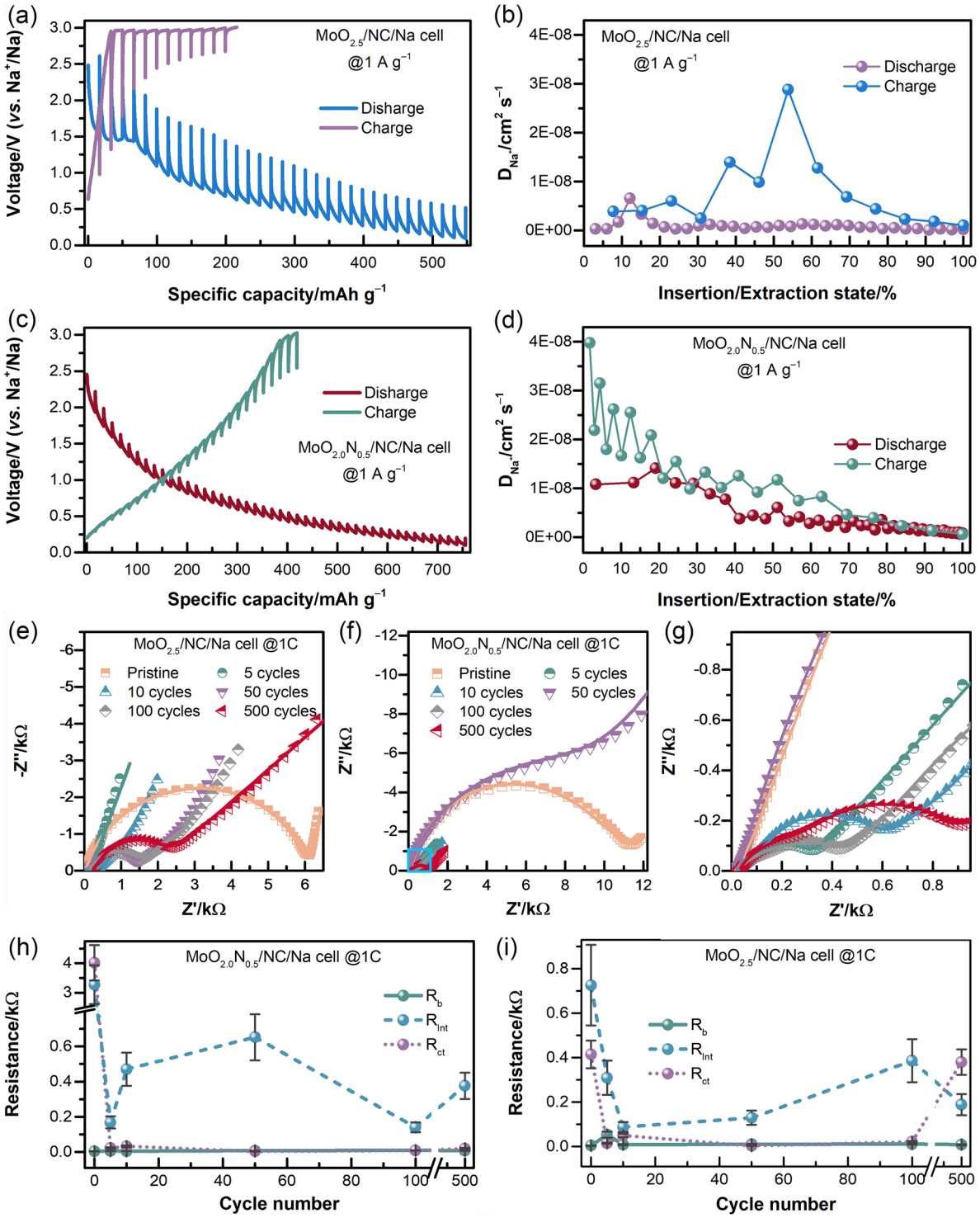

Fig. 6 GITT profiles (current pulse at 1 A g^{-1} for charging/discharging with 20 min relaxation) for **a** $MoO_{2.5}$/NC and **c** $MoO_{2.0}N_{0.5}$/NC, and corresponding sodium-ion diffusion coefficient of **b** $MoO_{2.5}$/NC and **d** $MoO_{2.0}N_{0.5}$/NC electrodes. Nyquist plots of **e** $MoO_{2.5}$/NC, **f–g** $MoO_{2.0}N_{0.5}$/NC; the resistance of the cells as functions of cycle number at 1 A $g.^{-1}$: **h** $MoO_{2.5}$/NC, and **i** $MoO_{2.0}N_{0.5}$/NC

https://doi.org/10.1007/s40820-022-00893-7

The Nyquist plots are shown in Fig. 6e–g. The Nyquist plots are fitting by an equivalent circuit shown in Fig. S12 and the obtained values of resistance are listed in Table S3. The EIS test results of the fully discharging process demonstrated that the R_b of the $MoO_{2.0}N_{0.5}$/NC/Na cells is maintained at 4.3–8.0 Ω (Table S3), and no evident change can be observed, indicating that the electrochemical reaction process of $MoO_{2.0}N_{0.5}$/NC is reversible. In the early stage, the decrease R_{ct} is possible due to the influence of SEI film. In the later stage, the R_b and R_{ct} of $MoO_{2.0}N_{0.5}$/NC are smaller than that of $MoO_{2.5}$/NC, indicating that $MoO_{2.0}N_{0.5}$/NC electrodes have the faster electron transfer rate (*i.e.,* the higher conductivity) and more stable nanosheet structure [51, 52]. The R_{int} of $MoO_{2.5}$/NC/Na and $MoO_{2.0}N_{0.5}$/NC/Na cells decreases first, and slightly fluctuates around 0.3 Ω, indicating sodium ion between the electrode materials and current collector has no significant difference [53].

Figure S13 shows the Bode plots of $MoO_{2.0}N_{0.5}$/NC and $MoO_{2.5}$/NC after various cycles with fully discharged. The Nyquist plots consist of two integrated semicircles at high and medium frequency range and an almost vertical line at low-frequency range (Fig. 6e–g). The semicircles are attributed to interfacial resistance and bulk resistance, while the vertical line at low-frequency range is assigned to sodium-ion diffusion [53]. As shown in Fig. S14a, there is one peak between 1 and 100 kHz, while there are two peaks at this frequency range, which can be explained that $MoO_{2.0}N_{0.5}$/NC has higher specific surface area than $MoO_{2.5}$/NC and is line with analysis on N_2-sorption isotherms, resulting in a higher surface activity and forming a thicker SEI layer at ~ 100 kHz [54]. The main difference between $MoO_{2.0}N_{0.5}$/NC and $MoO_{2.5}$/NC is that $MoO_{2.0}N_{0.5}$/NC has a peak at ~ 1 kHz, which is contributed to the better capacity of electron migration. Moreover, the angle phase of $MoO_{2.0}N_{0.5}$/NC at low-frequency region is slightly smaller than that of $MoO_{2.5}$/NC, illustrating that $MoO_{2.0}N_{0.5}$/NC has a faster sodium-ion diffusion in the electrodes [39].

4 Conclusion

In summary, we have demonstrated a two-step self-templating strategy for the synthesis of a novel hybrid architecture composed of $MoO_{2.0}N_{0.5}$ atomic nanoclusters bonded in nanosheets of N-doped carbon hierarchical hollow microspheres ($MoO_{2.0}N_{0.5}$/NC). The synthetic method can readily regulate the composition and structure of hybrid materials. With the inherent advantages of $MoO_{2.0}N_{0.5}$ atomic nanoclusters and the unique physicochemical characteristic of the three-dimensional hybrid host, the $MoO_{2.0}N_{0.5}$/NC anode empowers with both prolonged lifespan and enhanced rate capability, which satisfies the requirement of anode materials for the commercialization of sodium storage. This work may provide a feasible synthesis solution and structural perspective of transition metal nitrides atomic nanoclusters to be applied for sodium-ion batteries.

Acknowledgements The authors gratefully acknowledge the financial supports provided by the National Natural Science Foundation of China (U21A2077, 21971145, 21871164), the Taishan Scholar Project Foundation of Shandong Province (ts20190908), the Natural Science Foundation of Shandong Province (ZR2021ZD05, ZR2019MB024), Young Scholars Program of Shandong University (2017WLJH15), and Anhui Kemi Machinery Technology Co., Ltd. for providing a Teflon-lined stainless steel autoclave.

Funding Open access funding provided by Shanghai Jiao Tong University.

Supplementary Information The online version contains supplementary material available at https://doi.org/10.1007/s40820-022-00893-7.

References

1. C. Wang, L. Liu, S. Zhao, Y. Liu, Y. Yang et al., Tuning local chemistry of P2 layered–oxide cathode for high energy and long cycles of sodium–ion battery. Nat. Commun. **12**, 2256 (2021). https://doi.org/10.1038/s41467-021-22523-3

2. G. Zhu, X. Tian, H.C. Tai, Y.Y. Li, J. Li et al., Rechargeable Na/Cl_2 and Li/Cl_2 batteries. Nature **596**, 525–530 (2021). https://doi.org/10.1038/s41586-021-03757-z
3. M. Huang, Y. Chu, B. Xi, N. Shi, B. Duan et al., TiO_2-based heterostructures with different mechanism: a general synergistic effect toward high-performance sodium storage. Small **16**(42), 2004054 (2020). https://doi.org/10.1002/smll.202004054
4. C. Zhu, P. Kopold, P.A.V. Aken, J. Maier, Y. Yu, High power–high energy sodium battery based on threefold interpenetrating network. Adv. Mater. **28**(12), 2409–2416 (2016). https://doi.org/10.1002/adma.201505943
5. Y. Zhang, X. Xia, B. Liu, S. Deng, D. Xie et al., Multiscale graphene–based materials for applications in sodium ion batteries. Adv. Energy Mater. **9**(8), 1803342 (2019). https://doi.org/10.1002/aenm.201803342
6. M. Huang, B. Xi, N. Shi, J. Feng, Y. Qian et al., Quantum–matter Bi/TiO_2 heterostructure embedded in N–doped porous carbon nanosheets for enhanced sodium storage. Small Struct. **2**(4), 2000085 (2021). https://doi.org/10.1002/sstr.202000085
7. X. Sun, L. Wang, C. Li, D. Wang, I. Sikandar et al., Dandelion–like Bi_2S_3/rGO hierarchical microspheres as high–performance anodes for potassium–ion and half/full sodium-ion batteries. Nano Res. **14**, 4696–4703 (2021). https://doi.org/10.1007/s12274-021-3407-y
8. H. Li, H. Zhang, T. Diemant, R.J. Behm, D. Geiger et al., Reversible copper sulfide conversion in nonflammable trimethyl phosphate electrolytes for safe sodium–ion batteries. Small Struct. **2**(8), 2100035 (2021). https://doi.org/10.1002/sstr.202100035
9. M. Huang, B. Xi, Z. Feng, F. Wu, D. Wei et al., New insights into the electrochemistry superiority of liquid Na–K alloy in metal batteries. Small **15**(12), 1804916 (2019). https://doi.org/10.1002/smll.201804916
10. Z.L. Xu, G. Yoon, K.Y. Park, H. Park, O. Tamwattana et al., Tailoring sodium intercalation in graphite for high energy and power sodium ion batteries. Nat. Commun. **10**, 2598 (2019). https://doi.org/10.1038/s41467-019-10551-z
11. M. Chen, Z. Wang, Y. Wang, Y. Li, Q. Chen et al., Sodium–ion storage mechanisms and design strategies of molybdenum–based materials: a review. Appl. Mater. Today **23**(6), 100985 (2021). https://doi.org/10.1016/j.apmt.2021.100985
12. Y. Jiang, J. Dong, S. Tan, Q. Wei, F. Xiong et al., Surface pseudocapacitance of mesoporous Mo_3N_2 nanowire anode toward reversible high–rate sodium–ion storage. J. Energy Chem. **55**, 295–303 (2021). https://doi.org/10.1016/j.jechem.2020.07.011
13. N. Zheng, G. Jiang, X. Chen, J. Mao, N. Jiang et al., Battery separators functionalized with edge-rich MoS_2/C hollow microspheres for the uniform deposition of Li_2S in high–performance lithium–sulfur batteries. Nano-Micro Lett. **11**, 43 (2019). https://doi.org/10.1007/s40820-019-0275-z
14. B. Li, B. Xi, Z. Feng, Y. Lin, J. Liu et al., Hierarchical porous nanosheets constructed by graphene-coated, interconnected TiO_2 nanoparticles for ultrafast sodium storage. Adv. Mater. **30**(10), 1705788 (2018). https://doi.org/10.1002/adma.201705788
15. H. Luo, M. Cao, J. Cao, M. Zhang, S. Tan et al., Cocoon silk–derived, hierarchically porous carbon as anode for highly robust potassium–ion hybrid capacitors. Nano-Micro Lett. **12**, 113 (2020). https://doi.org/10.1007/s40820-020-00454-w
16. S. Qiu, L. Xiao, M.L. Sushko, K.S. Han, Y. Shao et al., Manipulating adsorption–insertion mechanisms in nanostructured carbon materials for high–efficiency sodium ion storage. Adv. Energy Mater. **7**(17), 1700403 (2017). https://doi.org/10.1002/aenm.201700403
17. W. Ye, F. Wu, N. Shi, H. Zhou, Q. Chi et al., Metal–semiconductor phase twinned hierarchical MoS_2 nanowires with expanded interlayers for sodium–ion batteries with ultralong cycle life. Small **16**(3), 1906607 (2020). https://doi.org/10.1002/smll.201906607
18. J. Chen, Y. Luo, W. Zhang, Y. Qiao, X. Cao et al., Tuning interface bridging between $MoSe_2$ and three–dimensional carbon framework by incorporation of MoC intermediate to boost lithium storage capability. Nano-Micro Lett. **12**, 171 (2020). https://doi.org/10.1007/s40820-020-00511-4
19. G. Jiang, Y. Qiu, Q. Lu, W. Zhuang, X. Xu et al., Mesoporous thin-wall molybdenum nitride for fast and stable Na/Li storage. ACS Appl. Mater. Interfaces **11**(44), 41188–41195 (2019). https://doi.org/10.1021/acsami.9b07060
20. S. Wang, H. Ge, S. Sun, J. Zhang, F. Liu et al., A new molybdenum nitride catalyst with rhombohedral MoS_2 structure for hydrogenation applications. J. Am. Chem. Soc. **137**(14), 4815–4822 (2015). https://doi.org/10.1021/jacs.5b01446
21. C. Zhu, A.L. Wang, W. Xiao, D. Chao, X. Zhang et al., In situ grown epitaxial heterojunction exhibits high-performance electrocatalytic water splitting. Adv. Mater. **30**(13), 1705516 (2018). https://doi.org/10.1002/adma.201705516
22. N. Shi, Y. Chu, B. Xi, M. Huang, W. Chen et al., Sandwich structures constructed by ZnSe⊂N-C@$MoSe_2$ located in graphene for efficient sodium storage. Adv. Energy Mater. **10**(41), 2002298 (2020). https://doi.org/10.1002/aenm.202002298
23. A.A. Herzing, C.J. Kiely, A.F. Carley, P. Landon, G.J. Hutchings, Identification of active gold nanoclusters on iron oxide supports for CO oxidation. Science **321**(5894), 1331–1335 (2008). https://doi.org/10.1126/science.1159639
24. N. Shi, B. Xi, M. Huang, F. Tian, W. Chen et al., One–step construction of MoS0 74Se1 26/N-doped carbon flower-like hierarchical microspheres with enhanced sodium storage. ACS Appl. Mater. Interfaces **11**, 44342–51 (2019). https://doi.org/10.1021/acsami.9b15769
25. C. Zhao, J. Kong, L. Yang, X. Yao, S.L. Phua et al., The dopamine–MoVI complexation–assisted large-scale aqueous synthesis of a single–layer MoS_2/carbon sandwich structure for ultrafast, long-life lithium–ion batteries. Chem. Commun. **50**(68), 9672 (2014). https://doi.org/10.1039/C4CC04099F
26. M.J. Sever, J.T. Weisser, J. Monahan, S. Srinivasan, J.J. Wilker, Metal–mediated cross–linking in the generation of a marine–mussel adhesive. Angew. Chem. Int. Ed. **43**(4), 448–450 (2004). https://doi.org/10.1002/anie.200352759
27. Y. Sun, Y. Zhou, Y. Zhu, Y. Shen, A. Xie, In–situ synthesis of petal–like MoO_2@MoN/NF heterojunction as both an

 https://doi.org/10.1007/s40820-022-00893-7

advanced binder–free anode and an electrocatalyst for lithium ion batteries and water splitting. ACS Sustain. Chem. Eng. **7**(10), 9153–9163 (2019). https://doi.org/10.1021/acssuschemeng.8b06321

28. X. Wang, J. Tian, X. Cheng, R. Na, D. Wang et al., Chitosan-Induced synthesis of hierarchical flower ridge–like MoS_2/N–doped carbon composites with enhanced lithium storage. ACS Appl. Mater. Interfaces **10**(42), 35953–35963 (2018). https://doi.org/10.1021/acsami.8b11593
29. L. Ma, X. Zhou, L. Xu, X. Xu, L. Zhang et al., Chitosan–assisted fabrication of ultrathin MoS_2/graphene heterostructures for Li–ion battery with excellent electrochemical performance. Electrochim. Acta **167**(10), 39–47 (2015). https://doi.org/10.1016/j.electacta.2015.03.129
30. F. Niu, J. Yang, N. Wang, D. Zhang, W. Fan et al., $MoSe_2$–covered N, P–doped carbon nanosheets as a long–life and high–rate anode material for sodium-ion batteries. Adv. Funct. Mater. **27**(23), 1700522 (2017). https://doi.org/10.1002/adfm.201700522
31. Y. Ai, Y. You, F. Wei, X. Jiang, Z. Han et al., Hollow bio–derived polymer nanospheres with ordered mesopores for sodium–ion battery. Nano-Micro Lett. **12**, 31 (2020). https://doi.org/10.1007/s40820-020-0370-1
32. R. Li, D. Rao, J. Zhou, G. Wu, G. Wang et al., Amorphization–induced surface electronic states modulation of cobaltous oxide nanosheets for lithium–sulfur batteries. Nat. Commun. **12**(5), 3102 (2021). https://doi.org/10.1038/s41467-021-23349-9
33. T.Y. Ma, J. Ran, S. Dai, M. Jaroniec, S.Z. Qiao, Phosphorus–doped graphitic carbon nitrides grown in situ on carbon–fiber paper: flexible and reversible oxygen electrodes. Angew. Chem. Int. Ed. **54**(15), 4646–4650 (2015). https://doi.org/10.1002/anie.201411125
34. L. Zhang, Q. Wang, R.K. Jian, D.Y. Wang, Bioinspired iron–loaded polydopamine nanospheres as green flame retardants for epoxy resin: via free radical scavenging and catalytic charring. J. Mater. Chem. A **8**(5), 2529–2538 (2020). https://doi.org/10.1039/C9TA11021F
35. I. Milošev, H.H. Strehblow, B. Navinšek, Comparison of TiN, ZrN and CrN hard nitride coatings: electrochemical and thermal oxidation. Thin Solid Films **303**(1–2), 246–254 (1997). https://doi.org/10.1016/S0040-6090(97)00069-2
36. S. Zhang, Y. Zeng, Z. Wang, J. Zhao, G. Dong, Glycerol-controlled synthesis of MoS_2 hierarchical architectures with well-tailored subunits and enhanced electrochemical performance for lithium ion batteries. Chem. Eng. J. **334**(2), 487–496 (2018). https://doi.org/10.1016/j.cej.2017.10.044
37. P. Xiao, M.A. Sk, L. Thia, X. Ge, R.J. Lim et al., Molybdenum phosphide as an efficient electrocatalyst for the hydrogen evolution reaction. Energy Environ. Sci. **7**(8), 2624–2629 (2014). https://doi.org/10.1039/C4EE00957F
38. P. He, Y. Fang, X.Y. Yu, X.W. Lou, Hierarchical nanotubes constructed by carbon-coated ultrathin SnS nanosheets for fast capacitive sodium storage. Angew. Chem. Int. Ed. **56**(40), 12202–12205 (2017). https://doi.org/10.1002/anie.201706652
39. J.C. Russell, V.A. Posey, J. Gray, R. May, D.A. Reed et al., High–performance organic pseudocapacitors via molecular contortion. Nat. Mater. **20**(4), 1136–1141 (2021). https://doi.org/10.1038/s41563-021-00954-z
40. Y. Zhang, Y. Huang, V. Srot, P.A. Aken, J. Maier et al., Enhanced pseudo–capacitive contributions to high–performance sodium storage in TiO_2/C nanofibers via double effects of sulfur modification. Nano-Micro Lett. **12**, 165 (2020). https://doi.org/10.1007/s40820-020-00506-1
41. S. Li, J. Qiu, C. Lai, M. Ling, H. Zhao et al., Surface capacitive contributions: towards high rate anode materials for sodium ion batteries. Nano Energy **12**(3), 224–230 (2015). https://doi.org/10.1016/j.nanoen.2014.12.032
42. H. Hou, C.E. Banks, M. Jing, Y. Zhang, X. Ji, Carbon quantum dots and their derivative 3D porous carbon frameworks for sodium-ion batteries with ultralong cycle life. Adv. Mater. **27**(47), 7861–7866 (2015). https://doi.org/10.1002/adma.201503816
43. M. Zhu, Z. Luo, A. Pan, H. Yang, T. Zhu et al., N–doped one–dimensional carbonaceous backbones supported $MoSe_2$ nanosheets as superior electrodes for energy storage and conversion. Chem. Eng. J. **334**(2), 2190–2200 (2018). https://doi.org/10.1016/j.cej.2017.11.158
44. C. Zhao, C. Yu, M. Zhang, H. Huang, S. Li et al., Ultrafine MoO_2–carbon microstructures enable ultralong–life power-type sodium ion storage by enhanced pseudocapacitance. Adv. Energy Mater. **7**(15), 1602880 (2017). https://doi.org/10.1002/aenm.201602880
45. B. Huang, S. Liu, X. Zhao, Y. Li, J. Yang et al., Enhancing sodium–ion storage performance of MoO_2/N–doped carbon through interfacial Mo–N–C bond. Sci. China Mater. **64**(6), 85–95 (2021). https://doi.org/10.1007/s40843-020-1370-x
46. C. Yang, M. Zhang, N. Kong, J. Lan, Y. Yu et al., Self–supported carbon nanofiber films with high–level nitrogen and phosphorus Co–doping for advanced lithium–ion and sodium–ion capacitors. ACS Sustain. Chem. Eng. **7**(10), 9291–9300 (2019). https://doi.org/10.1021/acssuschemeng.9b00300
47. D. Luo, J. Xu, Q. Guo, L. Fang, X. Zhu et al., Surface–dominated sodium storage towards high capacity and ultrastable anode material for sodium–ion batteries. Adv. Funct. Mater. **28**(47), 1805371 (2018). https://doi.org/10.1002/adfm.201805371
48. X. Jian, H. Wang, G. Rao, L. Jiang, H. Wang et al., Self–tunable ultrathin carbon nanocups as the electrode material of sodium–ion batteries with unprecedented capacity and stability. Chem. Eng. J. **364**(5), 578–588 (2019). https://doi.org/10.1016/j.cej.2019.02.003
49. J. Lee, S. Kim, J.H. Park, C. Jo, J. Chun et al., A small–strain niobium nitride anode with ordered mesopores for ultra–stable potassium–ion batteries. J. Mater. Chem. A **8**(6), 3119–3127 (2020). https://doi.org/10.1039/C9TA11663J
50. Q. Xia, H. Yang, M. Wang, M. Yang, Q. Guo et al., High energy and high power lithium-ion capacitors based on boron and nitrogen dual–doped 3D carbon nanofibers as

both cathode and anode. Adv. Energy Mater. **7**(22), 1701336 (2017). https://doi.org/10.1002/aenm.201701336

51. T. Ma, M. Zhang, H. Liu, Y. Wang, Synthesis of $CoMoO_4$–MoO_2 nanohybrids supported on graphene as high–efficiency catalyst for hydrogen evolution. J. Electroanal. Chem. **844**(1), 78–85 (2019). https://doi.org/10.1016/j.jelechem.2019.05.005
52. S. Wei, C. Wang, S. Chen, P. Zhang, K. Zhu et al., Dial the mechanism switch of VN from conversion to intercalation toward long cycling sodium–ion battery. Adv. Energy Mater. **10**(12), 1903712 (2020). https://doi.org/10.1002/aenm.201903712
53. X.Y. Qiu, Q.C. Zhuang, Q.Q. Zhang, R. Cao, Y.H. Qiang et al., Investigation of layered $LiNi_{1/3}Co_{1/3}Mn_{1/3}O_2$ cathode of lithium ion battery by electrochemical impedance spectroscopy. J. Electroanal. Chem. **687**(11), 35–44 (2012). https://doi.org/10.1016/j.jelechem.2012.09.027
54. C. Liang, L. Liu, Z. Jia, C. Dai, Y. Xiong, Synergy of Nyquist and Bode electrochemical impedance spectroscopy studies to particle size effect on the electrochemical properties of $LiNi_{0.5}Co_{0.2}Mn_{0.3}O_2$. Electrochim. Acta **186**(12), 413–419 (2015). https://doi.org/10.1016/j.electacta.2015.10.190

 https://doi.org/10.1007/s40820-022-00893-7